Catalysis Letters (2019) 149:3058–3065
https://doi.org/10.1007/s10562-019-02871-y

ZIF-67 Derived Hollow Structured Co_3O_4 Nanocatalysts: Tunable Synthetic Strategy Induced Enhanced Catalytic Performance

Changyu Zhang[1] · Wei Chu[2] · Ruiyu Jiang[1] · Lei Li[1] · Qilei Yang[3] · Yan Cao[1] · Jinlong Yan[1]

Received: 16 April 2019 / Accepted: 9 June 2019 / Published online: 22 June 2019

Abstract

Two different hollow structured Co_3O_4 micro-polyhedrons, derived from Zeolitic imidazolate frameworks (ZIF)-67 crystals, were fabricated by tuning the synthetic strategy (positive or reverse addition). The results demonstrate that the synthetic strategy significantly affect catalyst structure and properties. Compared with Co_3O_4-A nanocatalyst, the Co_3O_4-B nanocatalyst exhibit superior catalytic performance, showing 100% CO conversion at the conditions of T = 110 °C and SV = 30,000 h^{-1}. The higher catalytic performance could be attributed to its higher surface area, lower temperature reducibility, and abundant surface Co^{3+} and adsorbed oxygen.

Graphic Abstract

Two different hollow structured Co_3O_4 micro-polyhedrons, derived from Zeolitic imidazolate frameworks (ZIF)-67 crystals, were fabricated by tuning the synthetic strategy (positive or reverse addition). The Co_3O_4-B nanocatalyst exhibit superior catalytic performance, which should be attributed to its higher surface area, lower temperature reducibility, and abundant surface Co^{3+} and adsorbed oxygen.

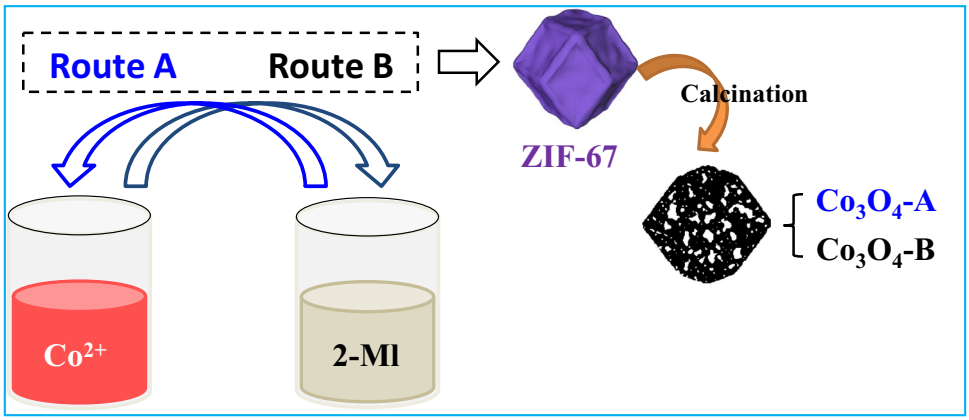

Keywords Synthetic strategy · Co_3O_4 nanocatalyst · Hollow structure · Zeolitic imidazolate frameworks · CO oxidation

1 Introduction

Hollow structured nanomaterials have attracted a broad interest in recent years due to their unique properties, such as high specific surface area, well-defined active site, inner void space, and tunable mass transfer rate [1, 2]. Controllable calcination of Metal–organic frameworks (MOFs) is a effective strategy for the preparation of hollow structural

✉ Lei Li
lee_ycit@yahoo.com

✉ Jinlong Yan
yjlyt@ycit.cn

Extended author information available on the last page of the article

materials [3–8]. And MOFs-derived hollow structural metal oxides, composing of special composites and developed pore channels, showed superior performance in catalysis and electrochemical applications. ZIF-67 derived hollow structured Co_3O_4 nanocomposites, have been reported with superior performance in electrochemical and gas sensing applications [9–13]. High porosity and inner voids endows it with high performance, which might be more meaningful in heterogeneous catalysis.

Co_3O_4 is considered as one of the most potential catalysts in CO oxidation due to its special morphology, structural and size effects [14–17]. Co_3O_4 nanobelts and nanocubes as model catalysts were well controllable synthesized to evaluate CO oxidation [14]. It was found that the Co_3O_4 nanobelts which have a predominance of exposed {011} planes are more active than Co_3O_4 nanocubes with exposed {001} planes. Compared with commercial Co_3O_4, mesoporous cobalt oxides showed improved activity in CO oxidation, which was ascribed to the lattice oxygen mobility of the catalysts promoted by the surface oxygen vacancy and large surface area. Besides, the particle size of Co_3O_4 nanocatalyst have shade an important effect on CO oxidation activity [16, 17]. Iablokov et al. [16] clarified the size effect of Co_3O_4 nanocatalyst in CO oxidation by well tuning the particle size from 3.5 to 12.2 nm. They found that the maximum reaction rates were observed for Co_3O_4 particles with a size in the range of 5–8 nm. These results clearly confirm that controlling the morphology of nanostructured cobalt oxides is beneficial for enhanced catalytic performance.

Herein, we prepared hollow structured Co_3O_4 nanocatalysts by annealing of ZIF-67 crystals in air atmosphere. Through tuning the synthetic strategy, two different Co_3O_4 nanocatalysts were fabricated. On the basis of catalytic performance for CO oxidation and various characterizations, a structure–activity relationship was well established.

2 Experiment

2.1 Synthesis

Porous Co_3O_4 hollow structural catalysts were prepared via a two-step route, involving the fabrication of Co-MOF (ZIF-67) nanocubes and the subsequent calcination treatment in air atmosphere. **Synthetic route A** $Co(NO_3)_2{\cdot}6H_2O$ (0.87 g) and 2-methylimidazole (1.97 g) were dissolved in 50 mL methanol respectively. Then the solution was mixed by pouring 2-methylimidazole solution into Co^{3+} solution under thoroughly stirring. The resulting mixture was aged for 24 h at room temperature. Then the purple precipitate was collected by centrifugation, washed with methanol three times, and dried at 80 °C for overnight. Finally, the as-prepared ZIF-67 precursors were heated to 350 °C with a heating rate of 1 °C·min^{-1}. The resulting product was denoted as Co_3O_4-350-A. **Synthetic route B** the synthetic process is similar to the above process. The only change is that the solution was mixed by pouring Co^{3+} solution into 2-methylimidazole solution under thoroughly stirring. And the final product was denoted as Co_3O_4-350-B.

2.2 Materials Characterization

The structural parameter, pore size distribution and N_2 adsorption isotherms of the samples were tested at liquid nitrogen temperature using an Autocorb apparatus. The samples were pretreated at 200 °C for 3 h before testing. The N_2 adsorption–desorption isotherm used the Barrett–Joyner–Halenda (BJH) method.

Thermogravimetric analysis (TGA) was conducted on SDT 2960 with a heating rate of 10 °C min^{-1} in air flow.

X-ray diffraction (XRD) patterns were obtained with a Bruker D8 diffractometer using Cu Kα radiation (λ = 1.540589 Å). The crystal size of samples was calculated from the width of diffraction pro- files, referring to the full width at half maximum (FWHM) of the crystalline phase using the Debye–Scherrer formula.

Scanning electron microscope (SEM) was performed on a JEOL JSM-6700F field emission SEM, which was operated at the accelerating voltage of 15 kV and the detector current of 10 mA. Transmission electron microscopy (TEM) was conducted on a JEOL JEM 2100 microscope operated at 200 kV.

The XPS patterns were measured on a PHI-5300/ESCA electronic energy spectrum at 300 W using Mg Kα X-rays as the excitation source. The data were processed by the XPS- PEAK software, and surface element contents were calculated through XPS peak areas. The inding energies (BE) of the elements were calibrated relative to the carbon impurity with a C 1 s at 284.8 eV. Laser Raman spectra were measured on a Renishaw Laser Raman spectrometer. Ar^+ (514.5 nm) and He–Cd lasers (325 nm) were used as the excitation source.

Temperature-programmed reduction (H_2-TPR) measurement was conducted on a TPDRO 1100 apparatus supplied by the Thermo-Finnigan company. Typically, 50 mg of the sample was heated from room temperature to 700 °C at a rate of 10 °C/min. A gas mixture of H_2/N_2 containing 5% H_2 (volume percentage) was used as a reductant at a flow rate of 20 mL/min.

Temperature-programmed desorption of CO (CO-TPD) was performed on the same apparatus with TCD detector. First, 0.1 g of samples was pretreated under N_2 flow at 120 °C for 1 h. After that, the temperature was cooled to 30 °C, and the flow gas was switched to 15% CO/He (30 mL/min). The CO adsorption continued at 30 °C for 1 h, and then were purged with He (30 mL/min) to remove

the physisorbed CO. The CO-TPD experiment was carried out by elevating temperature up from 30 to 300 °C with a heating rate of 10 °C/min.

2.3 Measurement of Catalytic Activity

The catalytic activity was measured by a fixed-bed flow microreactor at atmospheric pressure. In a typical experiment process, a 50 mg sample was loaded into a quartz tube (id = 6 mm) and then placed into a microreactor. The gas mixture of $CO/O_2/N_2$ (1.6:21.0:77.4) with a flow rate of 25 mL/min was introduced into the reactor, and the corresponding space velocity is 30,000 h^{-1}. Before test, the catalyst was pretreated in feed gas at 150 °C for 1 h. After cooling to room temperature, the CO oxidation was evaluated. The CO oxidation reaction was stabilized for 15 min, and the effluent gas from the reactor was analyzed by a gas chromatograph (GC-9860) equipped with a thermal conductivity detector and TDX-01 packed column.

3 Results and Discussion

Different hollow structured Co_3O_4 nanocomposites can be obtained through the calcination of ZIF-67 in air atmosphere via a tunable synthetic routes (Scheme 1). The powder X-ray diffraction (XRD) patterns of as-synthesized ZIF-67 sample is presented in Fig. 1a, which is matched well with the simulated and published XRD patterns, confirming the formation of pure ZIF-67 crystals [18]. Notable that the crystallinity of ZIF-67 prepared from synthetic route B is stronger than that from synthetic route A. This is in accordance with the SEM

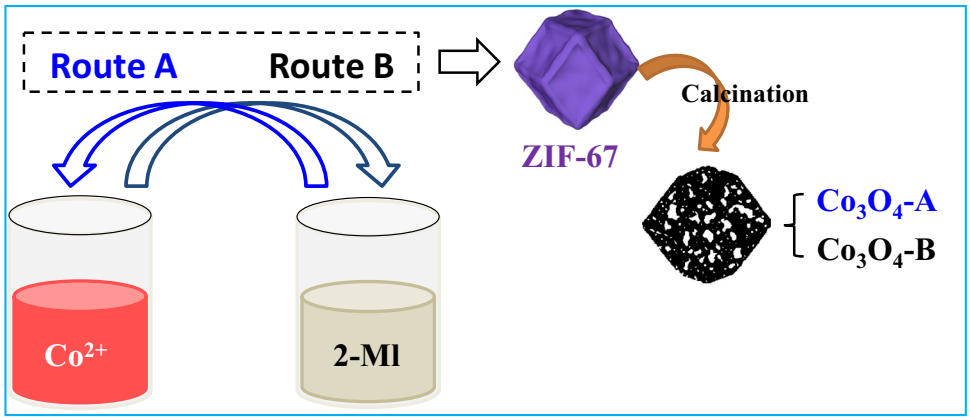

Scheme 1 Tunable synthetic strategy for hollow structured Co_3O_4 nanocomposites

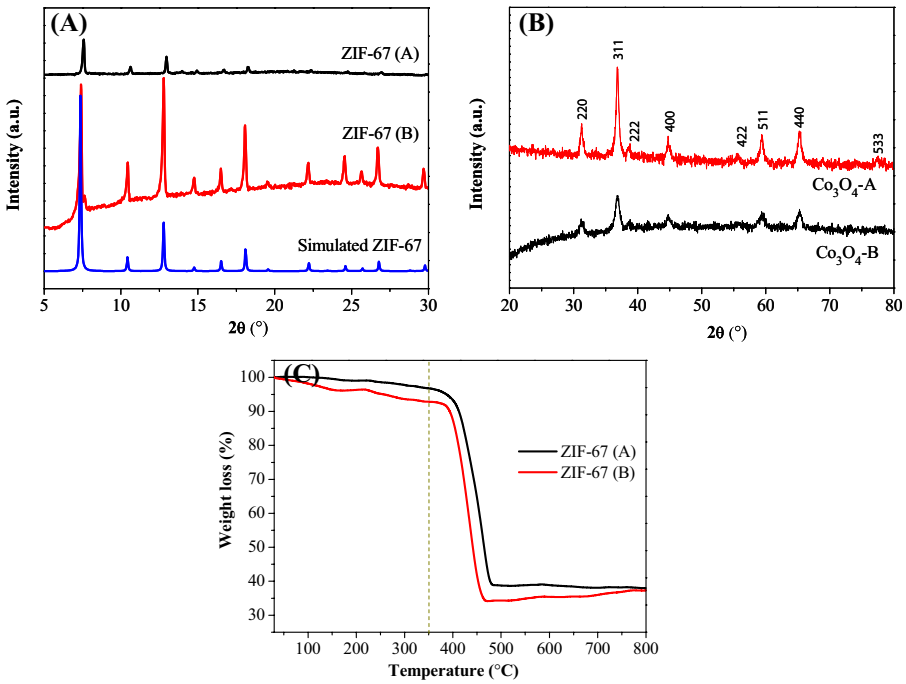

Fig. 1 XRD patterns of ZIF-67 crystals **a**, and **b** different hollow structured Co_3O_4 nanocomposites: Co_3O_4-A and Co_3O_4-B. **c** TGA curves of the ZIF-67(A) and ZIF-67(B) in air flow

results. After calcination in air atmosphere, the spinel-type Co_3O_4 species were obtained, further confirmed by XRD characterizations Fig. 1b. The diffraction peaks located at around 31.3°, 36.8°, 38.6°, 44.8°, 55.7°, 59.4°, 65.2° and 77.3° were recorded, assigning as the (220), (311), (222), (400), (422), (511), (440) and (533) crystalline planes of Co_3O_4 (JCPDS No. 01-073-1701). In addition, it can be observed that the intensity of reflection peaks is different over Co_3O_4-A to Co_3O_4-B samples, meaning that the primary crystallites in the products are different in particles size. According to the Scherrer equation, the mean crystallite size of the Co_3O_4-A and Co_3O_4-B samples are calculated to be 11.4 and 6.8 nm using the FWHMs of the (311) line of Co_3O_4 (Table 1). Additionally, through the comparison of the diffraction of ZIF-67 crystals and their derives, we can easily find that the ZIF-67(B) has good crystallinity, whereas its derives (Co_3O_4-B) show weak diffraction peaks, indicating smaller nanoparticles confirmed by TEM analyses. This result should be attributed to different synthetic route. In route A, 2-MI was poured into Co ions solution. Some uncoordinated 2-MI molecules would locate inside the structure of ZIF-67, and few residual Co ions might remain in the surface of ZIF-67, resulting in weak crystallinity of ZIF-67 and larger particle sizes of Co_3O_4. In route B, the reverse process was performed, some 2-MI might remain in the surface of ZIF-67, resulting in better crystallinity of ZIF-67 and smaller particle sizes of Co_3O_4.

The thermographic (TG) behaviors of the different ZIF-67 samples were measured in air flow. Seen from Fig. 1c, there exists a weak weight loss below 300 °C, which corresponds to the volatilization of methanol in the pores of ZIF-67. Above 300 °C, the weight loss becomes obvious, drops sharply at approximately 420 °C and finally flattens at approximately 480 °C. The latter weight loss might be attributed to the oxidation and decomposition of 2-methylimidazole. Notably, the weight loss of ZIF-67(B) took place at a relatively lower temperature that of ZIF-67(A). This result agrees well with the above analyses. For ZIF-67(B), some residual 2-MI remain on the surface of ZIF-67 during synthetic process, resulting in relatively lower decomposition temperature.

The morphology of the ZIF-67 samples and their corresponding calcined products are presents in Fig. 2. Whether synthetic A or B, the final ZIF-67 crystals are both composed of similar monodispersed rhombic dodecahedrons. By calcining the ZIF-67 crystals at 350 °C for 3 h, the typical morphology of Co_3O_4-A and Co_3O_4-B samples are presented in Fig. 2c and d. Clearly, the calcined particles retain the similar size and shape, along with inner hollow structure and rough porous shell. Some hollow structures are broken due to thermal effects. The microstructures of the prepared Co_3O_4-A and Co_3O_4-B samples are further characterized by HRTEM analysis (Fig. 3). Obviously, hollow structural dodecahedra, composed of numerous primary crystallites, are observed over the Co_3O_4-A and Co_3O_4-B samples (Fig. 3a, b, e and d). The average particle size of Co_3O_4-A (8.8 ± 2.6 nm) is larger than that of Co_3O_4-B samples (6.5 ± 1.2 nm) (Inset of Fig. 3b and e). This is consistent with above XRD results. Besides, typical (311) and (111) crystallographic planes of Co_3O_4 are also determined in Fig. 3c and f. Comparing Fig. 3a and d, it can be easily find that the formed Co_3O_4-A is assembled with core–shell structure, whereas the Co_3O_4-A has obvious hollow voids. This means that the different structure is originated from the different synthetic routes. In route A, more Co ions remaining in the surface of ZIF-67 are easily dropped into voids space during the oxidation process, forming an attached core.

N_2 sorption was also employed to characterize the surface areas and pore structure of Co_3O_4-A and Co_3O_4-B samples. Seen from Fig. 4a, both of the two samples display a characteristic Type IV adsorption isotherm with a H3-type hysteresis loop, indicating the presence of the mesoporous structure. A wide pore-size distribution is observed over these samples. The average pore sizes are 33.8 and 22.0 nm for Co_3O_4-A and Co_3O_4-B samples respectively (Table 1). This result is well consistent with TEM observations. Besides, their BET surface areas and pore properties are summarized in Table 1. The Co_3O_4-B sample exhibit much higher surface areas (72 m^2/g) than that of Co_3O_4-A sample (41.7 m^2/g). On basis of XRD and TEM results, the higher surface area is mainly originated from smaller primary particles of Co_3O_4, which generates more active sites for CO oxidation.

Table 1 BET surface areas, pore volume, pore sizes, particle sizes and the calculated specific rates of Co_3O_4-A and Co_3O_4-B catalysts

Sample	S_{BET} (m^2g^{-1})	Pore volume (cm^3g^{-1})	Pore size (nm)	Particle size[a]	Particle size[b]	Specific reaction rate[c] [$*10^{-8}$ mol/(m^2s)]
Co_3O_4-A	41.7	0.35	33.8	8.8	11.4	1.29
Co_3O_4-B	72.0	0.35	22.0	6.5	6.8	8.27

[a]Calculated from TEM images

[b]Calculated by Scherrer equation based on diffraction peak of (311)

[c]Reaction conditions: T = 110 °C, SV = 30,000 h^{-1}

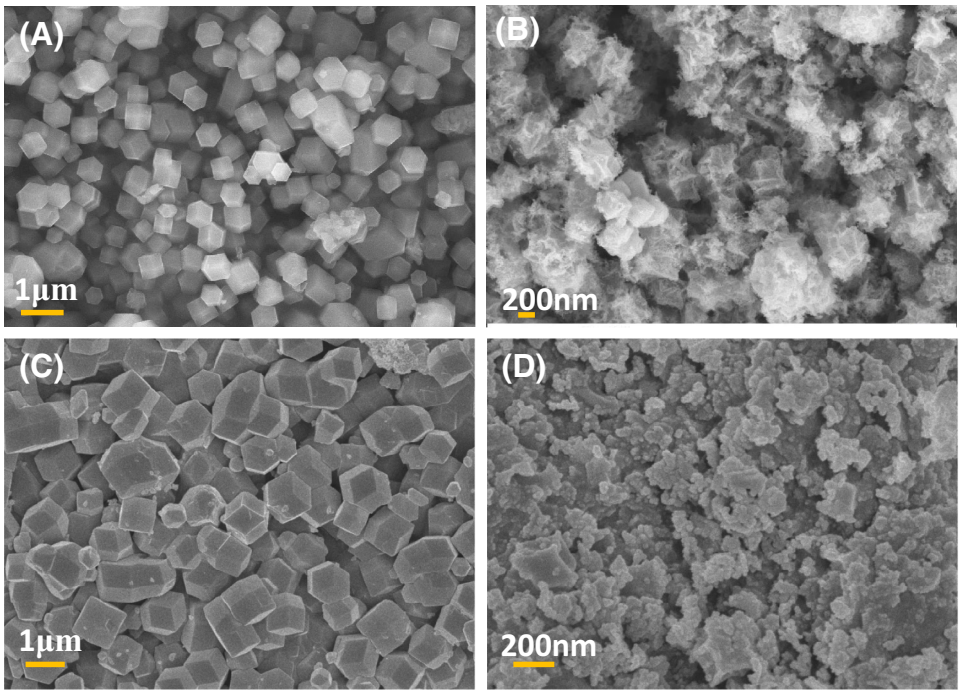

Fig. 2 SEM images of hollow structured Co_3O_4 nanocomposites: Co_3O_4-A (**a**, **b**) and Co_3O_4-B (**c**, **d**)

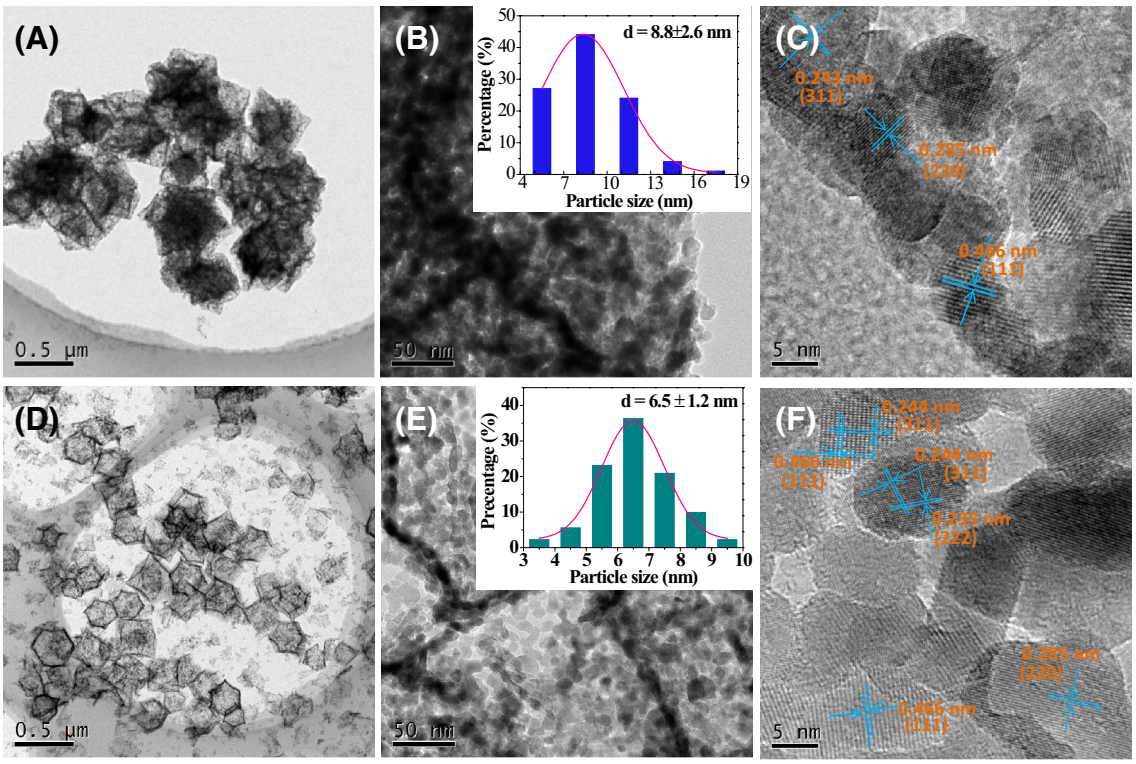

Fig. 3 HR(TEM) images of hollow structured Co_3O_4 nanocomposites: Co_3O_4-A (**a**, **b**, **c**) and Co_3O_4-B (**d**, **e**, **f**). The inset of B and E are their corresponding particle size distribution

H_2-TPR was performed to investigate the redox properties. Seen from Fig. 4b, the reduction profiles essentially present two obvious step-wise reduction peaks over Co_3O_4-A and Co_3O_4-B samples, which can be attributed to the reduction process of Co^{3+} to Co^{2+} and Co^{2+} to metallic Co^0 [19, 20]. Obviously, compared with Co_3O_4-A catalyst, the

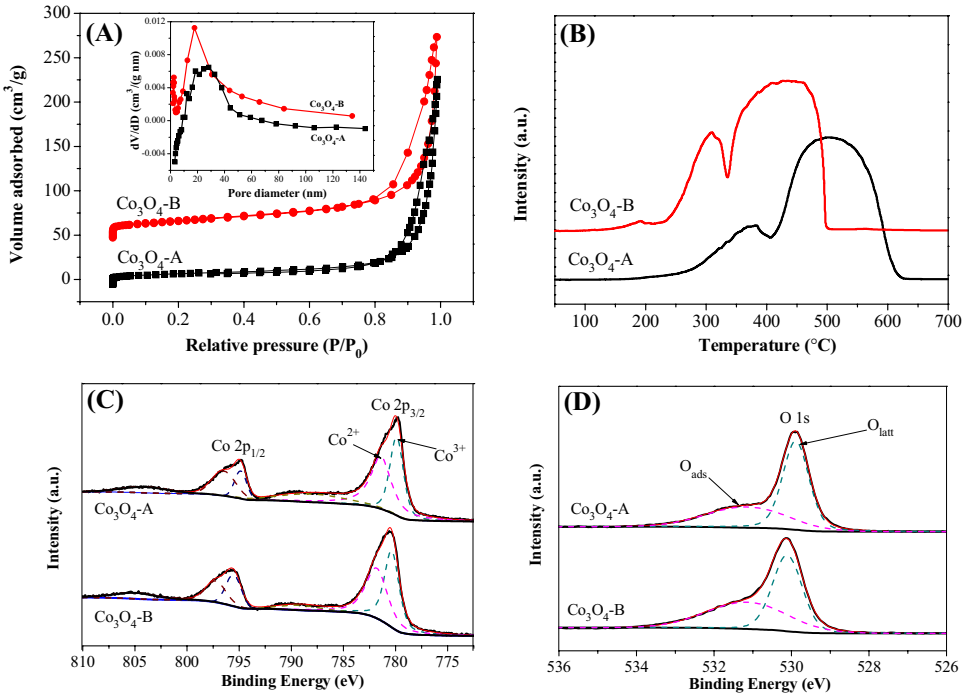

Fig. 4 Characterizations of hollow structured Co_3O_4 nanocomposites including Co_3O_4-A and Co_3O_4-B: **a** Nitrogen sorption isotherms and pore diameter distributions (Inset), **b** H_2-TPR profiles, and XPS spectra **c** Co 2p, **d** O1 s

Co_3O_4-B catalyst exhibit better reducibility at lower temperature, with one reduction peak at 310 °C and the other at 425 °C. It suggests that promoted oxygen mobility took place over Co_3O_4-B catalyst [21], resulting in better catalytic performance toward CO oxidation.

XPS was employed to obtain an insight into the surface composites and chemical state of different Co_3O_4-A and Co_3O_4-B samples, and the XPS spectra of Co 2p and O1 s are shown in Fig. 4c and d. The XPS datum are presented in Table 1. In Fig. 4c, two major with binding energies at ca. 780.0 and 795.0 eV corresponding to the $Co2p_{3/2}$ and $Co2p_{1/2}$, respectively [22, 23]. The Co $2P_{2/3}$ peak is deconvoluted into two components peaks Co^{3+} and Co^{2+}, and their binding energies are centered at around 780.0 and

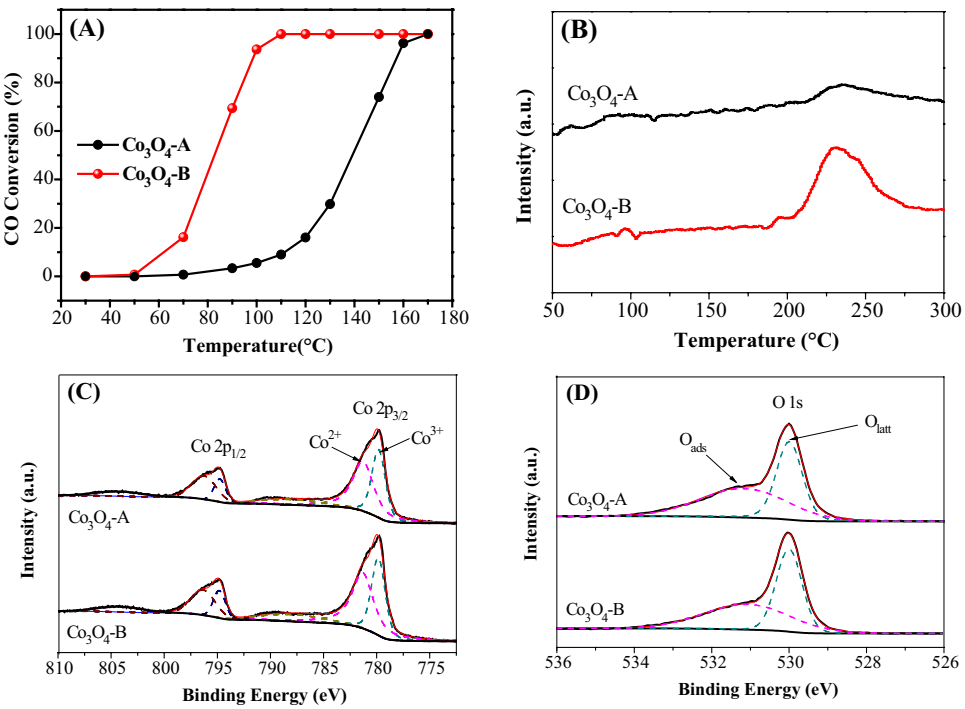

Fig. 5 **a** Catalytic activities of Co_3O_4-A and Co_3O_4-B samples in CO oxidation. **b** CO-TPD of Co_3O_4-A and Co_3O_4-B. And XPS spectra **c** Co 2p, **d** O1 s of the Co_3O_4-A and Co_3O_4-B after reaction

Table 2 XPS fitting results of Co_3O_4-A and Co_3O_4-B catalysts before and after reaction

Sample	Before reaction				After reaction			
	Co at. %	O at. %	$Co^{3+}/(Co^{2+}+Co^{3+})$ %	$O_{ads}/(O_{ads}+O_{latt})$ %	Co at. %	O at. %	$Co^{3+}/(Co^{2+}+Co^{3+})$ %	$O_{ads}/(O_{ads}+O_{latt})$ %
Co_3O_4-A	37.37	62.63	33.8	43.8	33.34	66.66	41.1	57.0
Co_3O_4-B	33.67	66.33	47.3	51.3	35.91	64.09	43.0	52.3

781.5 eV. We found that the relative surface content of Co^{3+} in the Co_3O_4-B sample is 47.3%, which is larger than that in Co_3O_4-A sample (33.8%). This result conforms to the H_2-TPR results. Figure 4c shows the O1 s XPS spectra of the contrast Co_3O_4-A and Co_3O_4-B catalysts, which can be fitted into three components peaks at ca. 530.1 and 531.5 eV. The two components peaks are sequentially ascribed to surface lattice oxygen (O_{latt}) species and surface adsorption oxygen (O_{ads}) respectively [24]. It can be seen that the relative surface content of O_{ads} in Co_3O_4-B (51.3%) is larger than that in Co_3O_4-B (43.8%). Thus, the surface contents of Co^{3+} and O_{ads} are obviously influenced by preparation method. According to previous studies [25, 26], more abundant of surface Co^{3+} and O_{ads} species contributed to higher catalytic performance. This finding is well in agreement with our study.

Figure 5a shows the catalytic activities of CO oxidation as a function of reaction temperature for Co_3O_4-A and Co_3O_4-B catalysts. It can be observed that there exhibit a large difference between Co_3O_4-A and Co_3O_4-B catalysts. And a complete 100% CO conversion took place at 110 °C for Co_3O_4-B catalyst, which is lower than that for Co_3O_4-A catalyst ($T_{100}=170$ °C). The calculated specific rates at 110 °C are presented in Table 1. The specific rates are 1.29×10^{-8} and 8.27×10^{-8} mol/(m^2s) for Co_3O_4-A and Co_3O_4-B respectively. It can be seen that the Co_3O_4-B catalyst has 7 times higher reaction rate than that of the Co_3O_4-A catalyst. Besides the contribution of surface area to activity, the surface concentrations of Co^{3+} and oxygen vacancies also contribute to higher activity. On the basis of above characterizations, there is no significant difference in morphology. As we know, CO species are adsorbed on the surface-exposed Co^{3+} sites and react with weakly bound oxygen species such as superoxide ion (O^{2-}) to form CO_2 [27]. The CO-TPD results are shown in Fig. 5b. It indicates that the Co_3O_4-B sample has more CO chemisorption uptakes, corresponding to abundant surface Co^{3+} contents. The active oxygen species are formed on surface oxygen vacancies which are increased by pretreatment in a reducing or oxidizing atmosphere [27, 28]. The higher catalytic performance of Co_3O_4-B catalyst, which can be attributed to higher surface area, lower temperature reducibility, and abundant surface Co^{3+} and adsorbed oxygen. Additionally, the used catalysts after reaction were further characterized by XPS techniques (Fig. 5c and d). By comparing the catalysts before and after reaction, we observe that the surface contents of Co^{3+} and adsorption oxygen (O_{ads}) exhibit an obvious rise for Co_3O_4-A catalyst, whereas there are only a slight decrease for Co_3O_4-A catalyst. It indicates that different treatments (e.g. reaction atmosphere) can effectively tune the surface chemical components at above 150 °C [27]. Especially for Co_3O_4-A catalyst, surface oxygen vacancies increase significantly after reaction, leading to more surface adsorbed oxygen. Partial adjacent Co^{2+} were also oxidized to Co^{3+}, as showed in Table 2.

4 Conclusions

In summary, two different hollow structured Co_3O_4 nanocatalyst were facilely prepared by tuning synthetic strategy. The results indicate that preparation method plays an important effect on CO oxidation activities. The superior Co_3O_4-B nanocatalyst exhibit higher performance and 100% CO conversion at 110 °C and 30,000 h^{-1}. The higher catalytic performance should be attributed to higher surface area, lower temperature reducibility, and abundant surface Co^{3+} and adsorbed oxygen. The results provide a scientific basis for the design of Co_3O_4-based oxidation catalysts.

Acknowledgements This work was supported by the National Natural Science Foundation of China (21503184), the Natural Science Foundation of the Jiangsu Higher Education Institutions of China (18KJA610004), and the Natural Science Foundation of Jiangsu Province-General Program (BK20171273).

References

1. Wang X, Feng JI, Bai Y, Zhang Q, Yin Y (2016) Chem Rev 116(18):10983–11060
2. Zhu W, Chen Z, Pan Y, Dai R, Wu Y, Zhuang Z, Li Y (2018) Adv Mater. https://doi.org/10.1002/adma.201800426
3. Zhang L, Wu HB, Lou XW (2013) J Am Chem Soc 135(29):10664–10672
4. Furukawa H, Cordova KE, O'Keeffe M, Yaghi OM (2013) Science 341(6149):1230444
5. Dang S, Zhu QL, Xu Q (2018) Nat Rev Mater 3(1):17075
6. Xia W, Mahmood A, Zou R, Xu Q (2015) Energy Environ Sci 8(7):1837–1866

7. Shieh FK, Wang SC, Yen CI, Wu CC, Dutta S, Chou LY, Tsung CK (2015) J Am Chem Soc 137(13):4276–4279
8. Chen JE, Fan MS, Chen YL, Deng YH, Kim JH, Alamri HR, Wu KCW (2017) Chem A Eur J 23(54):13284–13288
9. Lü Y, Zhan W, He Y, Wang Y, Kong X, Kuang Q, Zheng L (2014) ACS Appl Mater Interfaces 6(6):4186–4195
10. Li S, Peng S, Huang L, Cui X, Al-Enizi AM, Zheng G (2016) ACS Appl Mater Interfaces 8(32):20534–20539
11. Kaneti YV, Dutta S, Hossain MS, Shiddiky MJ, Tung KL, Shieh FK, Yamauchi Y (2017) Adv Mater 29(38):1700213
12. Zhou S, Ye Z, Hu S, Hao C, Wang X, Huang C, Wu F (2018) Nanoscale 10(33):15771–15781
13. Zhong G, Liu D, Zhang J (2018) J Mater Chem A 6(5):1887–1899
14. Hu L, Sun K, Peng Q, Xu B, Li Y (2010) Nano Res 3(5):363–368
15. Li Y, Shen W (2014) Chem Soc Rev 43(5):1543–1574
16. Iablokov V, Barbosa R, Pollefeyt G, Van Driessche I, Chenakin S, Kruse N (2015) ACS Catal 5(10):5714–5718
17. Li L, Yao Y, Tang Z, Ji W, Dai Y, Shen X (2016) J Nanosci Nanotechnol 16(7):7573–7578
18. Banerjee R, Phan A, Wang B, Knobler C, Furukawa H, O'Keeffe M et al (2008) Science 319:939
19. Ma CY, Mu Z, Li JJ, Jin YG, Cheng J, Lu GQ, Qiao SZ (2010) J Am Chem Soc 132(8):2608–2613
20. Wang J, Yang N, Tang H, Dong Z, Jin Q, Yang M, Wang D (2013) Angew Chem Int Ed 125(25):6545–6548
21. Luo JY, Meng M, Zha YQ, Guo LHJ (2008) Phys Chem C 112(23):8694–8701
22. Liu B, Liu Y, Hou H, Liu Y, Wang Q, Zhang J (2015) Catal Sci Technol 5(12):5139–5152
23. Bai G, Dai H, Deng J, Liu Y, Wang F, Zhao Z, Au CT (2013) Appl Catal A 450:42–49
24. Song W, Poyraz AS, Meng Y, Ren Z, Chen SY, Suib SL (2014) Chem Mater 26(15):4629–4639
25. Ren Q, Mo S, Peng R, Feng Z, Zhang M, Chen L, Ye D (2018) J Mater Chem A 6(2):498–509
26. Bai B, Li J (2014) ACS Catal 4(8):2753–2762
27. Yu YB, Takei T, Ohashi H, He H, Zhang XL, Haruta M (2009) J Catal 267:121–128
28. Widmann D, Leppelt R, Behm RJ (2007) J Catal 251:437–442

Affiliations

Changyu Zhang[1] · Wei Chu[2] · Ruiyu Jiang[1] · Lei Li[1] · Qilei Yang[3] · Yan Cao[1] · Jinlong Yan[1]

[1] School of Environmental Science and Engineering, Yancheng Institute of Technology, Yancheng 224051, China

[2] Department of Chemical Engineering, Sichuan University, Chengdu 610065, China

[3] State Key Joint Laboratory of Environment Simulation and Pollution Control, School of Environment, Tsinghua University, Beijing 100084, China